Fabrication of Add–Drop Filters Based on Frequency-Matched Microring Resonators

Tymon Barwicz, *Member, OSA*, Miloš A. Popović, *Student Member, IEEE, Student Member, OSA*, Michael R. Watts, *Member, OSA*, Peter T. Rakich, Erich P. Ippen, *Fellow, IEEE, Fellow, OSA*, and Henry I. Smith, *Fellow, IEEE, Member, OSA*

***Abstract*—Frequency mismatches between resonators significantly impact the spectral responses of coupled resonator filters, such as high-order microring filters. In this paper, techniques allowing fabrication of frequency-matched high-index-contrast resonators are proposed, demonstrated, and analyzed. The main approach consists of inducing small dimensional changes in the resonators through alteration of the electron-beam dose used to expose either the actual resonator on a wafer or its image on a lithographic mask to be later used in filter fabrication. Third-order microring filters fabricated in silicon-rich silicon nitride, with optical resonator frequencies matched to better than 1 GHz, are reported. To achieve this, the average ring-waveguide widths of the microrings are matched to within less than 26 pm of a desired relative width offset. Furthermore, optimization and calibration procedures allowing strict dimensional control and smooth sidewalls are presented. A 5-nm dimensional control is demonstrated, and the standard deviation of sidewall roughness is reduced to below 1.6 nm.**

***Index Terms*—Add–drop filters, coupling-induced frequency shifts (CIFS), electron-beam (e-beam) proximity effects, fabrication, microring resonators.**

I. Introduction

HIGH-INDEX-CONTRAST microring resonators allow for compact optical filters. Of particular interest to modern optical networks are optical add–drop filters that can be used for wavelength division multiplexing applications. Such add–drop filters must show, among other requirements, low input-to-drop-port loss (< 3 dB), high in-band extinction in the through port (> 30 dB), and a wide free spectral range (FSR) (> 30 nm). Frequency mismatches between resonators significantly alter the spectral responses of high-order microring filters [1]–[3]. In particular, the through response is the most affected and becomes inadequate for add–drop multiplexing applications. As a matter of fact, nearly all high-order microring filters reported in the literature have been aimed toward drop-only applications without mention of the through response [4]–[6].

In previous work [3], we found the frequency mismatch between microring resonators to be mainly due to coupling-induced frequency shifts (CIFS) [1], electron-beam (e-beam) proximity effects, and scanning e-beam lithography (SEBL) discretization errors. The first is an optical effect due to the perturbation at a coupler of the effective-index of the ring waveguide by the bus waveguide. The two others are lithographic imperfections. As a result, in a third-order microring filter, the middle microring exhibits a higher resonant frequency than the outer rings.

In this paper, techniques allowing fabrication of frequency-matched high-index-contrast resonators are proposed, demonstrated, and analyzed. The frequency matching is mainly performed by introducing slight and accurate dimensional changes in the resonators through alteration of the e-beam dose used to expose the actual resonator on a wafer or its image on a lithographic mask to be later used in filter fabrication. The expected frequency mismatch due to CIFS and e-beam proximity effects as well as the required e-beam-dose alteration for frequency matching are calculated. Calculated and experimentally observed parameters are compared, and excellent agreement is observed considering the complexity of the problem. Third-order microring filters fabricated by SEBL in silicon-rich silicon nitride (SiN) with resonators matched to better than 1 GHz are reported. The average ring-waveguide widths of these resonators are matched within 26 pm of a desired relative width offset. The frequency-matching technique allowed fabrication of third-order microring filters with 17-dB through-port extinction, which is the highest reported in the literature. When these filters are arranged in the cascaded configuration for which they were designed, the through extinction exceeds 30 dB [7].

A detailed treatment of resonance frequency control in microring filters is presented. The filter performance is quantitatively related to fabrication parameters. In addition, optimization and calibration procedures allowing strict dimensional control and smooth sidewalls are presented. A 5-nm dimensional control and a standard deviation of sidewall roughness below 1.6 nm are demonstrated. Furthermore, the e-beam writing strategy is optimized for microrings, and the e-beam proximity function is experimentally acquired.

II. Structures to be Fabricated

Our goal was to create add–drop filters with a 40-GHz bandwidth, less than 0.1-dB passband ripple, a 20-nm FSR, and a 30-dB rejection at the adjacent channels (assuming a 100-GHz channel spacing). Third-order filters were designed with a flattop (Chebyshev) drop-port response using known synthesis techniques [8]. The coupling gaps were obtained using

Manuscript received October 4, 2005; revised January 6, 2006. This work was supported in part by Pirelli, Milan, Italy.

The authors are with the Research Laboratory of Electronics, Massachusetts Institute of Technology, Cambridge, MA 02139 USA (e-mail: tymon@alum.mit.edu).

Digital Object Identifier 10.1109/JLT.2006.872298

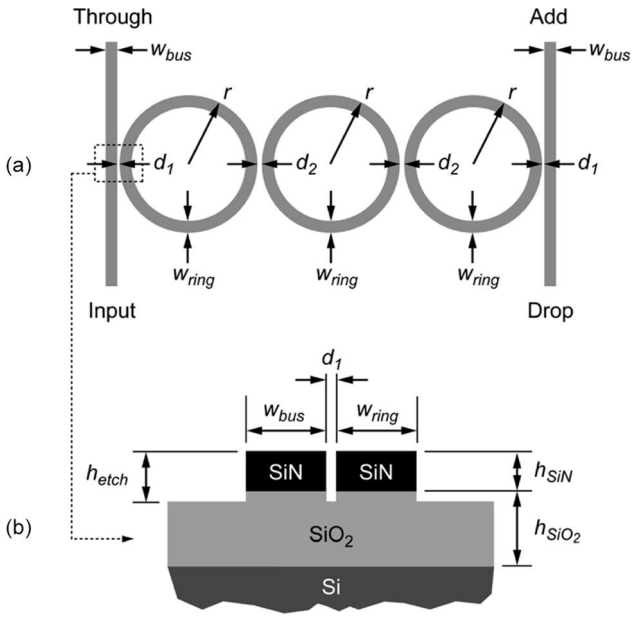

Fig. 1. Schematic of a series-coupled third-order microring filter. The microrings are designed to be alike. The actual parameters used are presented in Table I. (a) Top view and (b) cross section of the waveguides at the bus-to-ring coupling region.

TABLE I
DESIGNED FILTER PARAMETERS

Parameter	Filters with symmetric coupler design (SCD).	Filters with asymmetric coupler design (ACD).
h_{SiN}	400 nm	396 nm
h_{SiO2}	3 μm	3 μm
h_{etch}	500 nm	600 nm
n_{SiN}	2.200	2.181
n_{SiO2}	1.455	1.455
w_{bus}	804 nm	702 nm
w_{ring}	804 nm	900 nm
d_1	102 nm	120 nm
d_2	492 nm	372 nm
r	8004 nm	7998 nm

All lithographically defined dimensions were rounded to a 6 nm scanning-electron-beam-lithography step-size to ensure consistent discretization of patterns.

three-dimensional (3-D) finite-difference-time-domain (FDTD) simulations. The design details are reported in [7] and [9].

A series-coupled third-order microring filter is shown in Fig. 1. The waveguides are formed of an SiN core, a silicon oxide undercladding, and an air topcladding. The designed filter dimensions are shown in Table I. First, frequency-matched microring filters were demonstrated with a symmetric coupler design (SCD) employing identical bus-waveguide and ring-waveguide cross sections [9]. Then, the design was improved to further reduce the filter loss with an asymmetric coupler design (ACD) that reduced coupler scattering and a wider ring waveguide that reduced bending loss [7]. Coupler scattering was found to be the main source of filter loss in our previous work [3]. Fabrication of both microring structures is reported in the present paper.

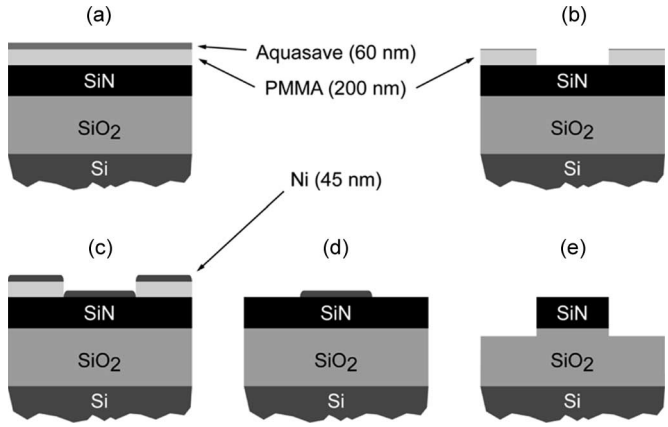

Fig. 2. Fabrication-process overview. (a) Initial multilayer formed from 3 μm of silicon oxide, 400 nm of silicon-rich silicon nitride (SiN), 200 nm of PMMA, and 60 nm of Aquasave [10]. (b) SEBL exposure, Aquasave removal, and PMMA development. (c) 45-nm Ni evaporation. (d) Liftoff. (e) Reactive-ion etching and Ni removal.

III. PROCESS OVERVIEW

The fabrication process is shown in Fig. 2. First, a Si wafer is thermally oxidized to form a 3-μm-layer of SiO_2. Then, a 400-nm-thick SiN layer is deposited by low-pressure chemical vapor deposition (LPCVD) in a vertical thermal reactor with a gas mixture of SiH_2Cl_2 and NH_3. The resulting SiN shows low stress and is often referred to as the low-stress nitride. Next, 200 nm of poly-methyl-methacrylate (PMMA) and 60 nm of Aquasave are spun on. PMMA is a positive e-beam resist while Aquasave [10] is a water-soluble conductive polymer used to prevent charging during SEBL. The PMMA is exposed at 30 keV using a Raith 150 SEBL system. The Aquasave is removed, and the PMMA developed. Next, 45 nm of Ni is evaporated on the structure, and a liftoff is performed by removing the nonexposed PMMA. Using the Ni as a hardmask, the waveguides are defined by conventional reactive-ion etching (RIE) with a gas mixture of CHF_3-O_2. To obtain an accurate etch depth, RIE is performed in several steps, in between which the etch depth is measured with a profilometer. Finally, the Ni is removed using a nitric-acid-based commercial wet Ni etchant, and the sample is prepared for optical characterization.

IV. SIDEWALL SMOOTHNESS

A. Liftoff Optimization

In the previous work, we found that liftoff is the fabrication step generating the most line-edge roughness (LER) [11]. This roughness is then transferred to the core material during RIE to form the biggest component of the sidewall roughness. At best, the LER of a lifted-off hardmask line will conform to the resist. However, coarse-material microstructure and coverage of the resist sidewall with the evaporated material worsen the LER of the hardmask. The material microstructure can be managed with appropriate e-beam evaporation parameters and surface cleanliness. The resist-sidewall coverage depends on the geometry of the e-beam evaporator and the angle of the resist sidewall. In most cases, the geometry of the evaporator cannot be altered and the resist-sidewall angle is the main liftoff-optimization parameter.

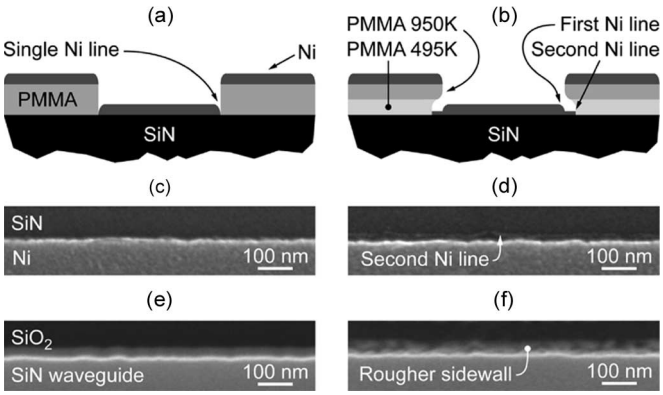

Fig. 3. Impact of resist profile on sidewall roughness. An undercut in the resist profile is desired but must be kept small. Schematic cross section of evaporated Ni on (a) single PMMA layer and (b) double PMMA layer. Top-view electron micrograph of resulting Ni liftoff for (c) single PMMA layer and (d) double PMMA layer. A second Ni line appears if the resist undercut is too strong. This second Ni line is partially sputtered during etching and contributes to increased sidewall roughness. Resulting waveguide sidewalls from a Ni hardmask (e) without and (f) with a secondary Ni line.

With sufficiently high e-beam dose, an undercut can be created in the resist. Electrons backscattered by the core material increase the dose delivered near the resist-dielectric interface. This undercut is helpful in reducing sidewall coverage and, thus, LER. A sharper undercut can be obtained by using a double-layer resist with the most sensitive resist on the bottom of the double layer. In our case, a double layer was investigated with two PMMA resists of different molecular weights: 950 kg/mol on top and 495 kg/mol on the bottom. The lower the molecular weight is, the more sensitive the PMMA.

Ni, Cr, and Al were investigated as hardmask materials. Of the three, Ni was found to provide the best liftoff results. Cr showed high-enough stress to pull on the PMMA and alter the sidewall angle while Al was too soft to be used as a hardmask for our applications. Surprisingly, the double-layer resist was found not to be useful for Ni liftoff. A sharp-resist profile is desired but the undercut needs to be small. As shown in Fig. 3, for strong undercuts, a thin Ni layer is formed on the edge of the hardmask. This layer gets partially sputtered during RIE and worsens the sidewall roughness. The formation of the thin layer can be explained by the sizeable energy of the e-beam evaporated Ni atoms providing them with the needed surface mobility to diffuse into the region shadowed by the upper part of the resist. This secondary Ni line is also formed when exposing a single resist layer with high electron doses.

In the present work, a single layer of 950-kg/mol PMMA was used. The e-beam dose was selected to be the highest one not triggering the formation of the thin secondary Ni layer. The PMMA was developed in a 2:1 mixture of isopropanol alcohol (IPA) to methyl iso-butyl ketone (MIBK) for 60 s at 21 °C. A lower portion of MIBK provides a higher contrast developer but increases the LER of the PMMA and should be avoided [12].

B. Reactive-Ion-Etching Optimization

To obtain smooth and vertical sidewalls, adequate sidewall polymerization (passivation) and hardmask erosion are required. The sidewall polymerization is controlled through the amount of O_2 in the CHF_3-O_2 gas mixture. The higher the O_2 content is, the weaker the polymerization. When the polymerization is too low, the sidewalls will be curved inwards and the hardmask undercut, which fosters mask erosion and roughness. When the polymerization is too high, the sidewalls will be straight but slanted with a wider base than top. A 16-to-3-sccm ratio of CHF_3 to O_2 was found optimal for SiN etching.

Mask erosion is known to be an important source of sidewall roughness. Surprisingly, it should not be strictly minimized. When using a Ni hardmask, the hardmask-to-SiN etching selectivity can be very high. We found that a controlled sputtering of the Ni hardmask can reduce the sidewall roughness presumably by polishing the hardmask during the RIE. Using a Plasmatherm 790 etcher, a 500-V bias resulting in a power of about 300 W was found to be optimal. It reduced the SiN:Ni etching ratio to about 50:1.

TABLE II
MEASURED SIDEWALL ROUGHNESS

Parameter	SCD Filters	ACD Filters
σ^2	3.5 nm^2	2.4 nm^2
L_c	30 nm	35 nm

Similar roughness with $\sigma^2 = 2.4\,\text{nm}^2$ and $L_c = 25\text{nm}$ was measured on previously reported filters in [3].

C. Resulting Sidewall Smoothness

The spectral density of the sidewall roughness was measured using the technique described in [11]. In most cases, the sidewall roughness can be well approximated by a one-dimensional (1-D) distribution with zero-mean called $f(z)$. It represents the excursion of the real edge from an idealized straight edge. The nature of roughness is described by the autocorrelation function of $f(z)$

$$R(u) = \langle f(z) f(z+u) \rangle$$

where z is the position along the waveguide, and the brackets represent the ensemble average. Typically, $R(u)$ can be well approximated [11], [13] by an exponential model

$$R(u) \approx \sigma^2 \exp\left(\frac{-|u|}{L_\text{c}}\right)$$

where σ^2 is the roughness variance, and L_c is the correlation length. A large L_c is indicative of strongly represented low spatial frequencies in the spectral density of roughness. As scattering losses due to sidewall roughness are triggered by these low spatial frequencies of roughness [14], the smaller the L_c is, the lower the scattering losses [15].

Measured values of σ^2 and L_c are presented in Table II. The roughness measurements were performed on bus-waveguides of actual filters. Fabrication of the SCD and ACD filters was separated by several months and the process was reoptimized to achieve smoother sidewalls on the later fabricated ACD filters.

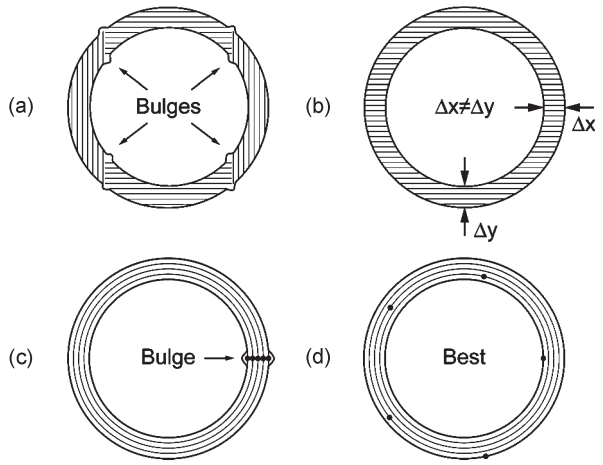

Fig. 4. E-beam vector-scanning strategies for microrings and observed problems in practice. (a) Default writing strategy in many vector-scan e-beam lithography systems. Bulges appear at the intersections between vertically and horizontally scanned lines. (b) Scanning the e-beam in only one axis removes the bulges but affects the width uniformity of the microrings. (c) Defining the microring with circular single pixel lines offers the best results but a bulge may appear near the starting/stopping point of the circular lines. (d) Angularly distributing the starting/stopping points removes the bulge.

The achieved sidewall smoothness is among the best reported [16], [17].

V. Pattern Accuracy

A. E-Beam Writing Strategy

SEBL systems are often designed with exposure of rectangular elements in mind (Manhattan geometry). When fabricating the smooth curves required in microphotonic applications, special attention must be given to the e-beam scanning strategy. In many vector-scan systems, a line is exposed by first deflecting the e-beam to a position at a given distance from one of the desired edges of the line to be exposed. Then, the e-beam is continuously scanned toward the edge of the line of interest. The e-beam is turned ON (blanker deactivated) at the time the scanning is expected to have reached the desired start of the line and turned OFF (blanker reactivated) at the time the scanning is expected to have reached the desired end of the line. Any error in the expected position of the e-beam in time during scanning will result in turning the beam ON and OFF at the wrong moment and will affect the position and the length of the line. These errors are particularly important in low-end SEBL systems like the Raith 150.

Fig. 4 shows four scanning strategies and the observed problems in practice. The scanning strategy can be controlled in most SEBLs by laying out the pattern with single-pixel lines. For best results, the pattern should be defined with circular single-pixel lines. As the SEBL makes errors at the connecting point where the line is started and ended, the starting points of the single-pixel lines should be angularly distributed to avoid formation of a bulge.

The geometry of the ring can also be affected by e-beam proximity effects as addressed in Section VI-D. To keep the ring smooth, standard proximity-correction algorithms should be avoided as they divide the ring in small areas of different doses, which can stress the SEBL toward higher pattern inaccuracy. Instead, this problem is better addressed by exposing dummy structures to render the dose distribution more uniform.

B. Dimensional Control

Strict dimensional control can be obtained by process calibration. Hence, it is limited by the repeatability of the fabrication process and the accuracy of the dimensional-measurement technique used for calibration. The e-beam dose is chosen for optimal sidewall smoothness. Then, the critical dimensions are measured, and the patterns are dimensionally biased in the SEBL layout to obtain the desired dimensions at device fabrication. To ensure consistent discretization of patterns, all dimensions must be chosen to be multiples of the SEBL step size. The dimensional repeatability of the fabrication process is enhanced when using a high-contrast resist and when measuring the e-beam current at regular intervals during long writes to ensure a uniform dose distribution across the wafer. Accurate dimensional measurements can be obtained by using the SEBL in scanning-electron-microscope (SEM) mode and calibrating the deflection of the e-beam to the movement of the interferometric stage. Such calibration can be accurate to 0.01% or better. Without it, usual dimensional measurement on standard SEMs can only be trusted to within a 5% error. In our case, the measurement accuracy is limited by mechanical vibrations during data acquisition and sidewall roughness. The measurement error is of the order of 5 nm on micrometer-size features.

Optical resonators are much more sensitive to dimensional variations than the dimensional-measurement accuracy. Some lithographic problems can only be observed through optical characterization of fabricated filters. For instance, we have observed a repeatable frequency mismatch of about 20 GHz between microring resonators in second-order filters. A similar problem was observed in fourth-order filters but not in third-order filters. We expect this to be mainly due to an error in the digital-to-analog converter of the Raith 150 resulting in an incorrect spacing between two or more horizontal lines of pixels near the middle of the write field.

C. Resulting Dimensional Control

The fabrication process was calibrated to provide a correct bus-to-ring coupling coefficient, which required an accurate coupling gap, bus-waveguide width, and ring-waveguide width in the bus-to-ring coupling region. Dimensional measurements of fabricated filters are presented in Table III. Strict dimensional control is demonstrated to within the measurement error ($\sim$ 6–8 nm for these measurements, can be as low as 5 nm for straight isolated waveguides). As e-beam proximity-correction algorithms were not applied, dimensional inaccuracies reaching 15 nm were observed on less critical parts of the structures.

Due to time limitations, the process calibration was performed by measuring the dimensions of the Ni hardmask and not of the etched waveguides. This approach was effective as the hardmask dimensions were at first indistinguishable from the waveguide dimensions. This was true until the RIE

TABLE III
MEASURED DIMENSIONS

Parameter	SCD Filters		ACD Filters	
	Measured dimension	Dimensional error	Measured dimension	Dimensional error
w_{bus}	804 nm	0 nm	704 nm	+2 nm
w_{ring}	802 nm	-2 nm	899 nm	-1 nm
d_1	103 nm	+1 nm	124 nm	+4 nm

The bus and ring waveguide widths were calibrated and measured at the bus-to-ring coupling region. Dimensions are reported at mid-height of the waveguides for the filters with symmetric coupler design and at the top of the waveguides for the filters with asymmetric coupler design. The measurement error is about 6-8 nm.

process was reoptimized to improve the sidewall smoothness before fabrication of the ACD filters. The resulting RIE process provided for a more slanted sidewall ($\sim 86^\circ$), and the hard-mask dimensions corresponded to dimensions at the top of the waveguides and not at the midheight of the waveguides. Therefore, in order to express the performance of the dimensional calibration itself, the dimensional measurements in Table III are reported at midheight of the waveguides for the SCD filters and at the top of the waveguides for the ACD filters. The latter waveguides were about 26 nm larger at the midheight than at the top when isolated. In the high-aspect-ratio bus-to-ring coupling gap, the sidewalls were more vertical and the coupling gap was reduced at midheight by about 16 nm. The difference is attributed to weaker sidewall polymerization in high-aspect-ratio trenches.

VI. RESONANCE FREQUENCY MATCHING

A. Frequency-Matching Strategy

Frequency mismatch between microring resonators can be due to CIFS [1], e-beam proximity effects, SEBL discretization errors, SEBL intrafield distortions, and SEBL digital-to-analog-converter errors.

As optical- and imprint-lithography masks are usually made by SEBL, all of the above mechanisms are expected to introduce frequency shifts even if the microrings are fabricated using optical or imprint lithography instead of SEBL. However, when optical projection lithography is used, the dimensional errors on the mask will be reduced by the demagnification factor of the projection system (usually 4 or 5×). Proximity-correction algorithms are typically applied in mask manufacturing. However, even if they help reduce frequency shifts due to e-beam proximity effects, they cannot eliminate these shifts as they correct the e-beam-dose distribution to first order only [18], which is insufficient for frequency matching.

The SEBL discretization errors can be eliminated by choosing all device dimensions to be multiples of the SEBL step size. All the remaining frequency-shift sources can be compensated by properly adjusting the middle-microring resonant frequency. The dimensional alteration required for such a correction is much smaller than the SEBL step size and cannot be obtained by changing the middle-ring dimensions in the SEBL layout.

Fig. 5. Frequency-matching strategies. (a) SEBL dose of the middle ring is increased to precisely widen the middle-ring waveguide. (b) Secondary nonresonant ring is introduced at the center of the middle ring to increase the effective index of the middle ring waveguide. Both methods lower the resonant frequency of the middle ring to match it to the outer rings. (a) is particularly useful if a maskless lithography technique, such as SEBL, is used and can be applied in either mask fabrication or direct device writing. (b) is particularly useful for photolithography or nanoimprint lithography when little control is exerted on the mask-manufacturing process.

However, such a small, precise, and accurate dimensional alteration can be introduced by changing the e-beam dose used at exposure of the middle microring. By increasing the middle-ring dose, the width of the ring waveguide is increased slightly and the middle-ring resonance frequency can be lowered to match it to the outer microrings. This dose compensation can be introduced when using direct-write SEBL or when fabricating a lithographic mask for optical or imprint lithography.

When optical or imprint lithography is used and little control is exerted on the mask fabrication, the middle-microring resonant frequency can be adjusted by changing the effective index of the ring waveguide without attempting to precisely correct its dimensions. A secondary nonresonant ring can be introduced in the center of the middle microring to increase its effective index and lower its resonance frequency to match it to the outer rings.

The two frequency-correction approaches are illustrated in Fig. 5. In the present work, only e-beam dose compensation was used.

B. Proximity Function

The exact e-beam dose compensation required for frequency matching of the microrings is best found empirically by fabricating and optically characterizing a number of filters with various dose compensations. However, to reduce the number of empirical iterations needed and better understand the underlying physical phenomena, knowledge of the e-beam proximity function is desired. The e-beam proximity function describes the spatial distribution of the resist exposure around the center of the e-beam. Its shape results from the interaction of the e-beam with matter. The knowledge of this shape allows us to estimate the frequency mismatch due to the e-beam proximity effects and the dose compensation needed for frequency matching. These two quantities cannot be usefully estimated from dimensional measurements, which lack the required accuracy.

The proximity function was found empirically using two different methods. First, large rings [Fig. 6(a)] were exposed with various inner radii and e-beam doses [19]. The rings were inspected with an SEM, and the minimum ring dose required to fully develop the resist in the middle of a ring with a given inner radius was noted. Second, isolated dots [Fig. 6(b)] were exposed with various e-beam doses, and their radii were measured

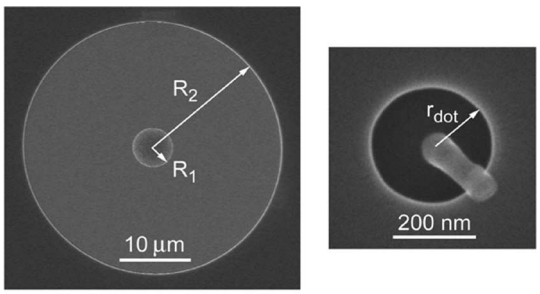

Fig. 6. Two empirical methods used to obtain the e-beam proximity function. (a) Large rings were exposed with various inner radii and doses. The lowest ring dose clearing the center of the ring was noted. (b) Dots were exposed at various doses, and their radii were measured. The pole in the middle of the dot (fallen on its side) is characteristic of PMMA exposed at high doses where it becomes highly cross linked and insoluble to the resist developer.

with an SEM [20]. All exposures were performed on the multilayer of interest [Fig. 2(a)] with a Raith 150 SEBL operating at 30 keV. The PMMA was developed with 3:1 IPA:MIBK, which is a higher contrast developer than the one used for microring fabrication, as resist contrast was more important for this application than line-edge smoothness. Then, the samples were coated with a thin (2–3 nm) layer of Au-Pd to prevent charging during the SEM analysis.

The proximity function $f(r)$ is a monotonically decreasing function normalized so

$$\int_0^\infty f(r)2\pi r dr = 1$$

where r is the distance from the center of the e-beam to the point of interest. Most often, it is assumed to follow a double-Gaussian model [21]

$$f_0(r) = \frac{1}{\pi(1+\eta)}\left(\frac{1}{\alpha^2}\exp\left(\frac{-r^2}{\alpha^2}\right) + \frac{\eta}{\beta^2}\exp\left(\frac{-r^2}{\beta^2}\right)\right) \tag{1}$$

where $\alpha < \beta$ and where the first Gaussian accounts for forward electron scattering and the second Gaussian accounts for backward electron scattering.

The experimental results obtained with the large rings are presented in Fig. 7(a). The required ring dose D to reach, at the center of the ring, the resist clearing dose D_0 is given by

$$D = \frac{D_0}{\int_{R_1}^{R_2} f(r)2\pi r dr} \simeq \frac{D_0}{\int_{R_1}^{\infty} f(r)2\pi r dr}, \qquad \text{for} \quad R_2 > 3\beta$$

where R_1 and R_2 are the inner and outer ring radii, respectively. Most often, R_2 is chosen to be large enough for the upper limit of the integration to be approximated by infinity. In the present experiments, $R_2 = 18\ \mu$m was used.

The experimental results obtained with the dots are presented in Fig. 7(b). The dot dose $d_{\rm dot}$ and the dot radius $r_{\rm dot}$ are related

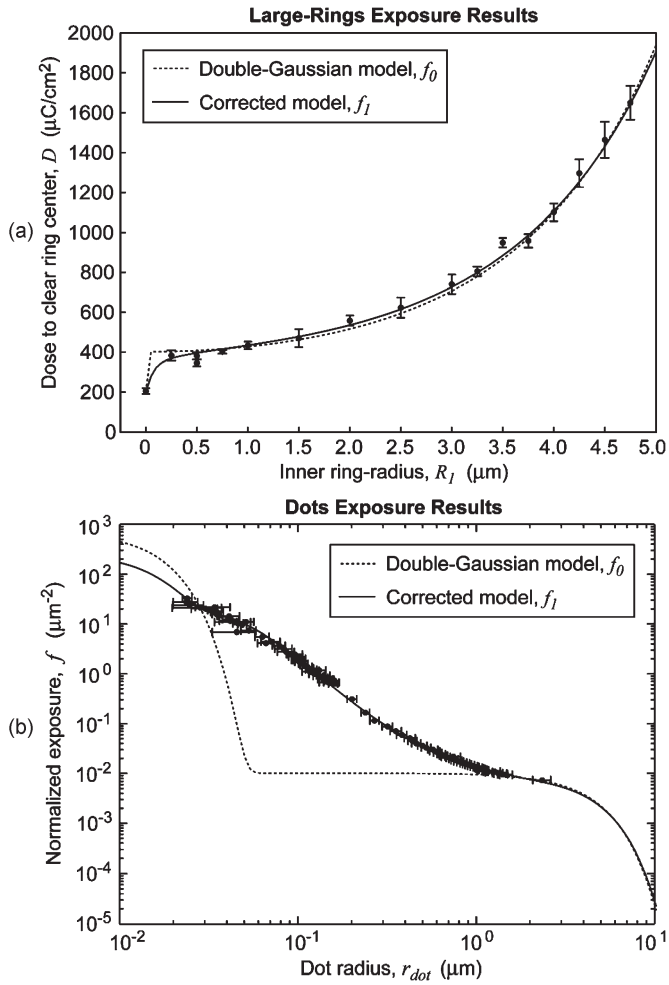

Fig. 7. Experimentally obtained e-beam proximity function. (a) Results obtained with large ring exposures and (b) results obtained with dot exposures. The standard double-Gaussian model of the e-beam proximity function is not appropriate, as seen in (b). The model was corrected with the tail function presented in (2). The fitted parameters are reported in Table IV.

to the proximity function by

$$f(r_{\rm dot}) = \frac{D_0}{d_{\rm dot}} \quad \left(10^{-8}\ \text{cm}^2/\mu\text{m}^2\right)$$

where $r_{\rm dot}$ is expressed in μm, $f(r)$ is expressed in μm^{-2}, D_0 is expressed in μC/cm^2, and $d_{\rm dot}$ is expressed in μC.

Exposing large rings was found to be particularly useful for probing the proximity function at long interaction lengths ($R_1 > 1\ \mu$m). For small R_1, identifying the needed ring dose accurately is difficult as a particle can be mistaken for remaining resist. On the other hand, exposing the dots was found particularly useful for short to medium interaction lengths ($40\ \text{nm} < r_{\rm dot} < 1\ \mu$m). For longer interactions, the exposure contrast becomes too low at the clearing dose for the edge of the PMMA to be well defined (an even higher contrast resist would be required). Below 40 nm, the measurements are also difficult as the feature size gets close to the resist resolution, and the shape of the dots is affected by imperfect stigmation of the e-beam.

The large rings experimental data were least square fit to the double-Gaussian model of (1). The best fit is shown with dotted

TABLE IV
E-BEAM PROXIMITY-FUNCTION FITTED PARAMETERS

Parameter	Double-Gaussian model $f_0(r)$	Corrected model $f_1(r)$
β	3.99 μm	4.08 μm
η	1.02	2.52
t_0		-4.935
t_1		-2.734
t_2		-0.786
t_3		-0.565
t_4		-0.108

$\alpha = 0.015\ \mu m$ was assumed from simulation data provided by the SEBL manufacturer. t_4, t_3, t_2, t_1, and t_0 are provided for r expressed in μm. The 95% confidence interval on β and η is ±0.1 μm and ±0.1, respectively. Parameters are provided with a sufficient number of digits to accurately reproduce Fig. 7.

lines in Fig. 7(a) and (b). The fitted parameters are presented in Table IV. As $f(r)$ could not be probed at sufficiently short interaction lengths, $\alpha = 0.015\ \mu$m was assumed from simulation data provided by the SEBL manufacturer. The resulting fit looks acceptable in Fig. 7(a) but in Fig. 7(b), where the discrepancy is amplified by the logarithmic scale, the double-Gaussian model looks obviously inappropriate. A similar tail in the proximity function has been reported in [20], where it was found to be possibly due to scattering in the resist, high-energy secondary electrons, and tails in the incident e-beam distribution. In addition, the proximity function was simulated in [22] for the multilayer and e-beam energy of interest, and a similar tail was observed.

The double-Gaussian model can be corrected by adding a tail function $\tau(r)$. Then, the proximity function becomes

$$f_1(r) = \frac{f_0(r) + \tau(r)}{1 + \int_0^\infty \tau(r) 2\pi r dr}.$$

From Fig. 7(b), we can see that the tail could be fit to a polynomial in logarithmic space. In fact, a simple exponential is not sufficient. Hence, we choose the tail function to be of the form

$$\tau(r) = \exp\left(t_4(\ln(r))^4 + t_3(\ln(r))^3 + t_2(\ln(r))^2 + t_1(\ln(r)) + t_0\right) \tag{2}$$

where t_4, t_3, t_2, t_1, and t_0 are the fitting parameters. The best fit to this corrected double-Gaussian model is shown with the solid lines in Fig. 7(a) and (b). The fitted parameters are reported in Table IV.

C. Fast Proximity-Effect Computation

To define arbitrary structures, the SEBL exposes sets of discreet points (pixels). The dose at a given location $D(x, y)$ will be given by the summation of the contributions of all exposed points weighted by the proximity function

$$D(x,y) = \sum_i q_i f_1\left(\sqrt{(x-x_i)^2 + (y-y_i)^2}\right) \tag{3}$$

where x and y define the location at which the dose is sought, x_i and y_i define the position of an exposed point, and q_i is the dose delivered at that point. When the SEBL step size is smaller than the proximity-function parameter α, (3) is well approximated by a two-dimensional (2-D) convolution

$$D(x,y) = Q \otimes\otimes f_1 = \int_{-\infty}^{+\infty}\int_{-\infty}^{+\infty} Q(x',y') f_1\left(\sqrt{(x-x')^2 + (y-y')^2}\right) dx'dy'$$

where Q is the dose profile laid out in the SEBL. For arbitrary patterns, the 2-D convolution needs to be computed numerically. However, even with the best algorithms, a numerical 2-D convolution requires a large number of operations and is not well suited for computation of small dimensional changes in large structures like microring resonators. For microring filters, the following semi-analytical method can greatly simplify the computational problem. It takes advantage of the fact that microring filters are formed of 1-D elements. Microrings are 1-D elements in cylindrical coordinates and infinitely long and straight bus waveguides are 1-D elements in Cartesian coordinates. Bus waveguides oriented along the y axis can be assumed infinitely long and straight if they extend straight to more than 3β ($\sim$ 12 μm) above and below y. Then, the dose profile resulting from exposing with unit dose a bus waveguides oriented along the y axis and centered at the origin is given by

$$F_{\text{bus}}(x) = \int_{\frac{-w_{\text{bus}}}{2}}^{\frac{+w_{\text{bus}}}{2}} f(x-x')dx'$$

while the dose profile resulting from exposing with unit dose a microring centered at the origin is given by

$$F_{\text{ring}}(r) = \int_{R-w_{\text{ring}}}^{R}\int_0^{2\pi} f\left(\sqrt{r'^2 + r^2 - 2r'r\cos\theta'}\right) d\theta' r' dr'.$$

The above form of convolution in cylindrical coordinates is valid when the convolved functions are angularly invariant [23]. The complete dose profile is given by

$$D(x,y) = \sum_j Q_j F_{\text{bus}}(x - x_j) + \sum_k Q_k F_{\text{ring}}\left(\sqrt{(x-x_k)^2 + (y-y_k)^2}\right)$$

where Q_j and Q_k are the area doses defined in the SEBL layout for each element (ring or waveguide), x_j defines the middle of each bus waveguide, and x_k and y_k define the center of each microring.

D. Predicted Microring Shapes

Using the fast proximity-effects computation presented above, the dose profile was computed for the two filter structures addressed in this paper. The shape of the microrings and

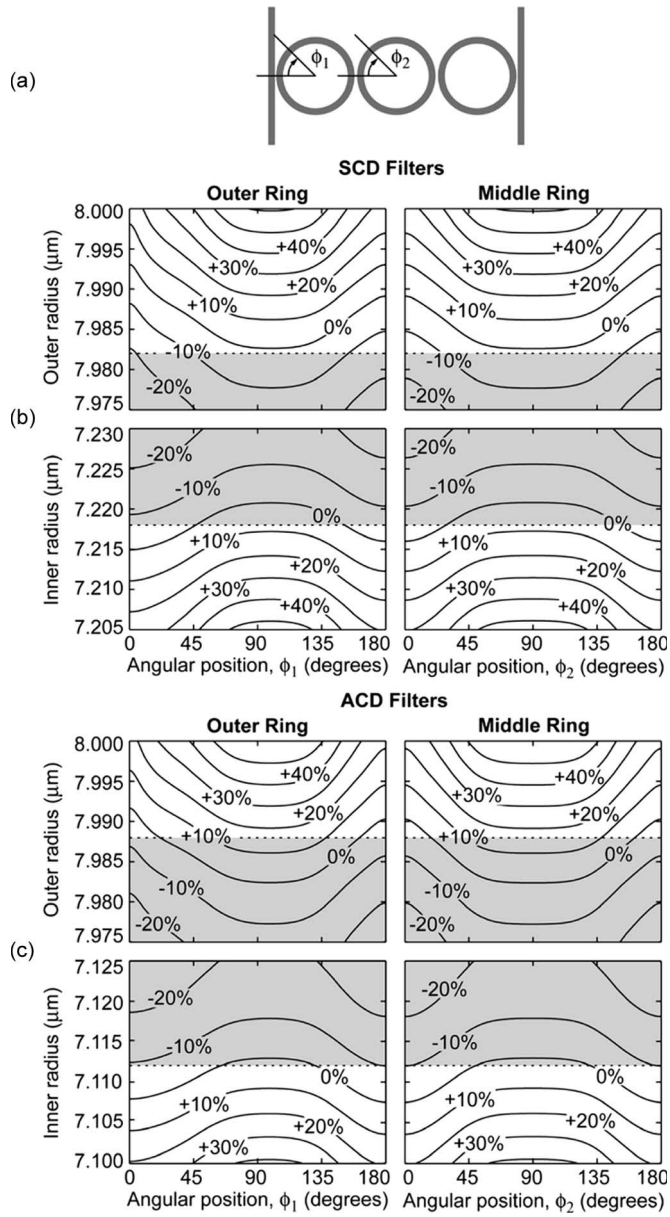

Fig. 8. Resist clearing-dose contours for various SEBL area doses expressed as relative offsets from the dose minimizing the width variations in all ring waveguides of a filter. The ring-waveguide edges will follow the clearing-dose contours but will be consistently offset by the fabrication process. The dotted lines represent the positions of the ring-waveguide edges in the SEBL layout and take into account the width bias used in fabrication. The shaded areas correspond to regions exposed by the SEBL. (a) Definition of angular positions along the outer and middle rings. (b) Clearing-dose contours for SCD filters. (c) Clearing-dose contours for ACD filters.

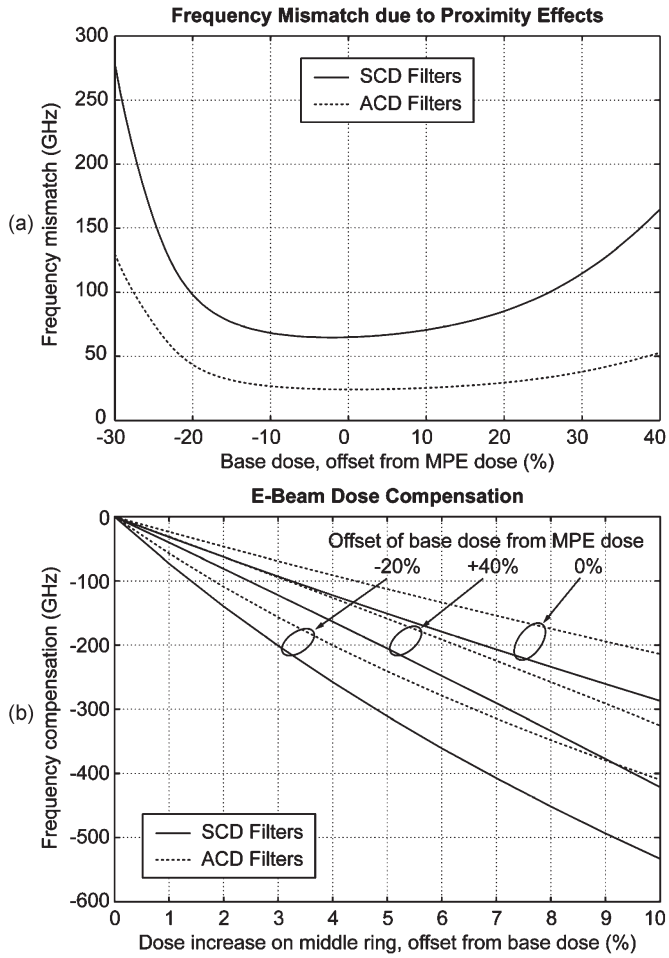

Fig. 9. (a) Predicted frequency mismatch between middle and outer microrings due to e-beam proximity effects. MPE dose is defined as the SEBL dose minimizing the width variation in all ring waveguides of a filter. (b) Predicted frequency compensation resulting from an increase of the SEBL dose on the middle ring. The base dose is the SEBL area dose used on all rings in (a) and on outer rings in (b).

all relative dimensions will follow approximately the contours of constant dose corresponding to the clearing dose of the resist. However, the absolute dimensions of the microrings will be consistently offset from these contours by the fabrication process.

The microring shape is a function of the SEBL area dose used. A given SEBL area dose [the minimum-proximity-effect (MPE) dose] will minimize the width variations in all microrings. In the present case, it is obtained when the SEBL area dose used is about three times the clearing dose of the resist. In Fig. 8, the clearing-dose contours are plotted for various SEBL doses, expressed as relative offsets from the MPE dose. As expected, the ring waveguides are wider for higher e-beam doses. The largest ring-waveguide widths are obtained near the small bus-to-ring coupling gaps while the smallest ring-waveguide widths are obtained near the top and bottom of the middle rings [in orientation of Fig. 8(a)]. The dose profile of each filter has two axes of symmetry (one vertical and one horizontal) going through the center of the middle ring of the filter.

When the same dose is used on middle and outer rings, the width of the middle ring is smaller than the width of the outer rings. Moreover, as the outer and inner radii are differently affected by proximity effects, the ring circumference will be larger in the outer rings than in the middle ring. These raise the resonant frequency of the middle ring and create a frequency mismatch with the outer rings. This frequency mismatch is a function of the SEBL area dose used as the shapes of the middle and outer rings are differently affected by a dose change. This dependence is presented in Fig. 9(a). The smallest frequency mismatch is obtained near the MPE dose. When the SEBL dose used differs significantly from the MPE dose, the frequency mismatch increases sharply due to a weaker

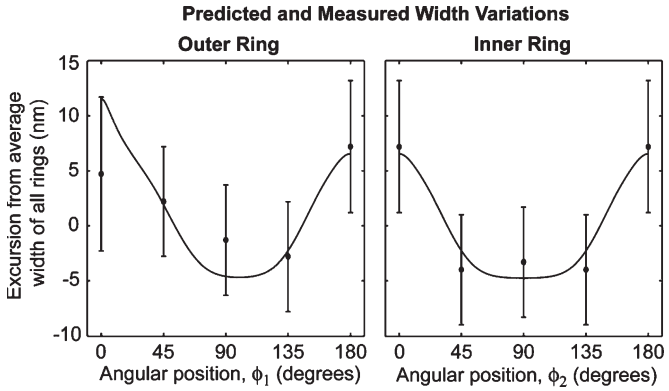

Fig. 10. Predicted and measured width variations in ring waveguides of SCD filters. The dimensional measurements were performed as explained in Section V-B. The filter is assumed to have two axes of symmetry (one vertical and one horizontal) going through the center of the middle ring. The angular positions used are defined in Fig. 8(a).

dose-profile gradient near the resist-clearing dose resulting in larger variations of the microring shapes. To correct for frequency mismatches due to proximity effects and all other repeatable sources, one can increase the dose on the middle ring to reduce its resonant frequency. The resulting frequency compensation is shown in Fig. 9(b). Note that the exact shapes of the outer and middle rings do not need to be the same, as only the resonant frequencies need to be equal. An estimate of the total frequency mismatch can be obtained by adding an estimate of the CIFS (usually obtained by FDTD electromagnetic simulations) to the frequency mismatch due to proximity effects of Fig. 9(a). Then, an estimate of the dose compensation required is obtained from Fig. 9(b).

A dose increase on the middle ring will lower not only the resonant frequency of the middle ring but also, through proximity effects, the resonant frequency of the outer rings. This phenomenon is taken into account in Fig. 9(b). For a given dose compensation, the outer rings' resonant frequency will be decreased by 3.0%–3.5% of the decrease of the middle ring resonant frequency.

E. Comparison of Predicted and Measured Dimensions

The width of fabricated microrings was measured in SCD filters at several angular positions using the method described in Section V-B. During fabrication, the SEBL area dose was chosen to minimize the sidewall roughness. Predicted microring shapes were obtained using an estimate of the clearing dose of the resist, allowing us to choose the appropriate dose contours. The actual dose employed was found to be close to the MPE dose. Predicted and measured angular-width variations are compared in Fig. 10. They agree within the measurement error and confirm the validity of our analysis. The worst agreement is observed near the bus-to-ring coupling gaps. It is believed to be due to the behavior of RIE in small trenches, where sidewall passivation is reduced leading to wider gaps than expected. Another source of possible disagreement between predicted and measured width variations is the finite chemical contrast of the resist. Resist edges would exactly follow the clearing-dose contours only if the resist exhibited infinite chemical contrast. Obviously, this is not the case in practice. However, it is generally an acceptable approximation for high-contrast resists, such as PMMA.

Error bars in Fig. 10 show that a useful estimate of the frequency mismatch cannot be obtained from dimensional measurements alone. For instance, in the SCD filters, a 5-nm measurement error on the ring-waveguide width corresponds to a 200-GHz error in the resonance frequency of the corresponding microring.

VII. Fabricated Frequency-Matched Filters

The exact dose compensation required for frequency matching was obtained empirically by fabricating and optically characterizing sets of filters with various dose compensations distributed around the expected compensation. The expected dose compensation was estimated as described in Section VI-D. The experimental results are summarized in Figs. 11 and 12. The observed and predicted frequency mismatches and required dose compensations are compared in Table V.

In Fig. 11, electron micrographs of frequency-matched SCD and ACD filters are shown along with spectral responses of filters with and without frequency compensation. As shown in Fig. 11(c), the filter response is overwhelmed by frequency shifts when dose compensation is not applied. With appropriate dose compensation, the frequency mismatches were reduced to below 1 and 2 GHz for SCD and ACD filters, respectively. This allowed the highest filter through-port rejection reported in the literature. The SCD and ACD filters showed 14 and 17 dB of through rejection, respectively. The drop-port passband ripple is also disturbed by the frequency mismatch. However, the through-port extinction is affected first and is overwhelmed before the passband's ripple becomes significant. In Fig. 11(d) and (e), the passband ripple is negligible, and the spectral oscillations are Fabry–Pérot fringes created by reflections at the chip facets.

The frequency compensation works mainly by offsetting the average ring width of the middle microring with respect to the outer microrings. Considering the sensitivity of the resonant frequency with variations of the ring-waveguide width and the frequency matching obtained, one finds that the average ring-waveguide widths are matched to a desired relative offset to better than 26 pm in SCD filters and to better than 68 pm in ACD filters.

The designed filter bandwidth was 40 GHz. The observed filter bandwidths were 30 and 42 GHz for the SCD and ACD filters, respectively. The improvement in bandwidth control in the ACD filters is due mainly to spectroscopic ellipsometer measurements of the SiN index and thickness being made prior to coupler design and having the design trimmed to the parameters of a given wafer chosen for fabrication. In SCD filters, the SiN thickness and index were chosen to be 400 and 2.20 nm, respectively. Then, matching these parameters in fabrication was attempted. The SiN thickness and index used in fabrication were 406 $\pm$ 1 nm and 2.189 $\pm$ 0.003, respectively. The difference between the designed and observed filter bandwidths is mainly due to a variation of the coupling

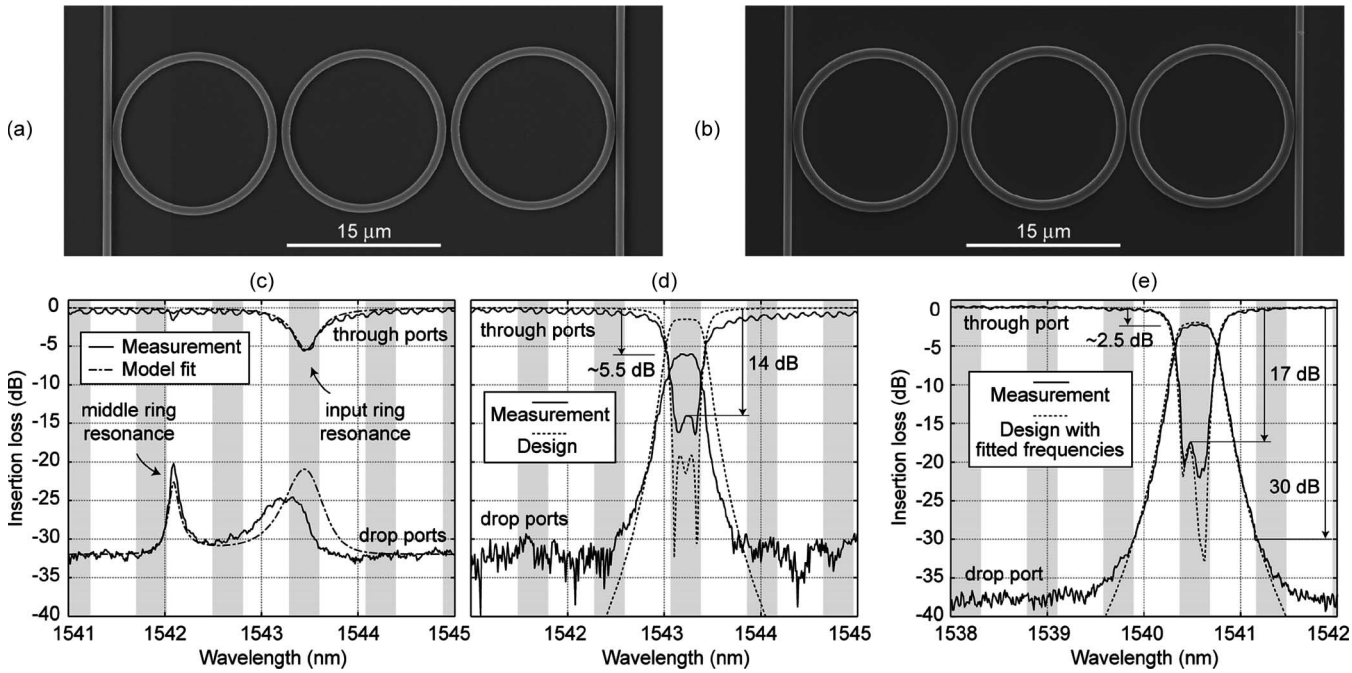

Fig. 11. Electron micrographs of fabricated frequency-matched (a) SCD filters and (b) ACD filters. Spectral responses of SCD filters (c) without dose compensation and (d) with a 4.5% e-beam dose increase in the middle ring. (e) Spectral response of an ACD filter with a 4.2% e-beam dose increase in the middle ring. As shown in (c), the filter response is overwhelmed by the frequency shifts when dose compensation is not applied. The predicted and required dose compensations are compared in Table V. The resonant frequencies of the microrings of the filters reported in (d) and (e) are matched to better than 1 and 2 GHz, respectively. The drop-port passband ripple introduced by such frequency mismatch is negligible, and the spectral oscillations seen in (d) and (e) are Fabry–Pérot fringes created by reflections at the chip facets. The ACD improved the filter drop loss by reducing coupler scattering, which is a significant source of loss identified in our previous work [3].

coefficients induced by the modest discrepancy between the designed and deposited SiN parameters.

The drop losses observed in SCD and ACD filters were ~ 5.5 and ~ 2.5 dB, respectively. The drop loss was improved by the ACD by reducing the coupler scattering, which is a significant source of loss identified in our previous work [3], and bend loss. The remaining 2.5-dB drop loss is due mainly to a propagation loss of about 9 dB/cm. Recently, fabrication of shallow-etched ridge waveguides in thick SiN films confirmed that the waveguide-propagation loss was mainly due to SiN material loss [24]. Based on the roughness measurement reported in Table II and on the calculations reported in [15], the scattering losses due to sidewall roughness are expected to be negligible in our filters.

In Fig. 12, the empirical relationships between frequency mismatch and dose compensation are presented. Each point on the graphs was obtained by fitting filter spectral responses, such as the one shown in Fig. 11(c), with an analytic filter model. Parabolic trend lines were introduced in the graphs. The empirical trends follow the calculated ones [shown in Fig. 9(b)] well at small dose compensations but level off at high dose compensations. The flattening of the empirical trend is difficult to explain. Most likely, it is not due to lithographic phenomena but is rather caused by subsequent processing (liftoff and RIE). The insets in Fig. 12 show the data point to trend-line excursions that cannot be explained by measurement and fitting errors. The frequency distribution is tighter for ACD filters than for SCD filters. The difference is mainly due to a better controlled fabrication process and a wider ring-waveguide width in ACD filters (see Table I). In fact, the wider the ring-waveguide is, the smaller the frequency shifts introduced by e-beam proximity effects are. Hence, there is a clear advantage in keeping the ring-waveguide as wide as possible.

Table V compares predicted and observed frequency mismatches and dose compensations. Considering the relative simplicity of the analysis when compared to the complexity of the problem, excellent agreement is observed. The calculated frequency mismatches take into account only the CIFS and the e-beam proximity effects. The difference between the calculated and observed mismatches can be explained by frequency-shift sources not taken into account in the calculations, such as SEBL intrafield distortions and SEBL digital-to-analog-converter errors. When looking at the calculated dose compensation required for the observed mismatch, a perfect agreement is observed for the SCD filters. For ACD filters, the dose compensation required is underestimated in calculation. This is due mainly to the flattening of the empirical dose-compensation trend shown in Fig. 12(b). This flattening is stronger in ACD filters than in SCD filters. The main difference in fabrication between the two filter structures is in the RIE process, where stronger sidewall passivation was used in ACD filters than in SCD filters (as discussed in Section V-C).

Filter-to-filter frequency variations were also studied. When three identical ACD filters are spaced by 100 μm, their resonant frequencies can be matched to 2–5 GHz [7]. When the filter-to-filter spacing reaches a centimeter, the frequency can differ by up to ~ 240 GHz [25]. By analyzing the form of the drift with filter position, we found that it was due mainly to the

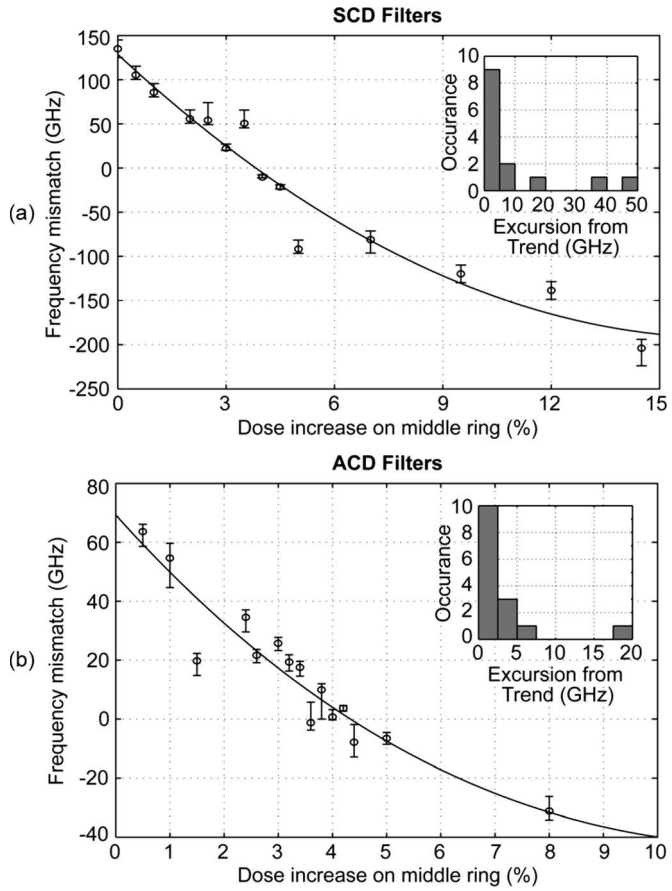

Fig. 12. Empirical relationships between frequency mismatch and dose compensation for (a) SCD filters and (b) ACD filters. Data points were obtained by fitting spectral responses, such as the one shown in Fig. 11(c). Parabolic trend lines were introduced in the graphs. The insets show the data point to trend-line excursions that cannot be explained by measurement and fitting errors. A better controlled fabrication process and wider ring-waveguide widths allowed for a tighter distribution of frequencies in ACD filters.

variations in the SiN thickness. In fact, the resonant frequency will increase by $\sim$ 70 GHz for a decrease of 1 nm in SiN thickness.

Wafer-to-wafer frequency variations could not be empirically estimated as the sample size was not statistically significant. However, the repeatability of the lithographic process can be assessed from Fig. 9. Assuming that the ratio of the base dose to the clearing dose can be controlled to 2% while the dose increase can be controlled to 0.05%, the relative frequencies can potentially be controlled to 1–2 GHz. This excludes the stochastic variations shown in Fig. 12.

VIII. Conclusion

We presented techniques allowing fabrication of frequency-matched high-index-contrast resonators, a detailed treatment of frequency control in microring resonators, and optimization and calibration procedures allowing strict dimensional control and smooth sidewalls. We reported third-order microring filters with resonator frequencies matched to 1 GHz. We demonstrated 5-nm dimensional control and a standard deviation of sidewall roughness below 1.6 nm. The techniques developed allowed fabrication of microring filters with low drop loss, good bandwidth control, and the highest through extinction reported in the literature. The techniques presented in this paper are of value for the fabrication of all types of high-index-contrast resonators.

TABLE V
Comparison of Calculated and Observed Frequency Mismatches

Parameter	SCD Filters	ACD Filters
Calculated mismatch due to e-beam proximity effects	70 GHz	30 GHz
Calculated coupling-induced frequency-shift (CIFS)	38 GHz	22 GHz
Total calculated frequency-mismatch	108 GHz	52 GHz
Observed frequency-mismatch (from trend lines)	130 GHz	70 GHz
Difference between observed and calculated mismatch	22 GHz	18 GHz
Calculated dose compensation required	3.6 %	2.2 %
Calculated dose compensation required for observed mismatch	4.3%	3.0 %
Observed dose-compensation required	4.0-4.5%	4.2-4.4%
Smallest frequency mismatch obtained	< 1 GHz	< 2 GHz
Matching of average ring-waveguide widths to ideal	< 26 pm	< 68 pm

Acknowledgment

The authors would like to thank F. Zhang for his help in troubleshooting the Raith 150 SEBL and L. Socci for his help in the optical characterization. This work made use of MIT's shared SEBL facility in the Research Laboratory of Electronics (SEBL at RLE).

References

[1] C. Manolatou, M. A. Popovic, P. T. Rakich, T. Barwicz, H. A. Haus, and E. P. Ippen, "Spectral anomalies due to coupling-induced frequency shifts in dielectric coupled resonator filters," in *Proc. Opt. Fiber Commun. Conf.*, Washington, DC, 2004, pp. 379–381.

[2] M. A. Popovic, C. Manolatou, and H. A. Haus, "Coupling-induced resonance frequency shifts in coupled dielectric multi-cavity filters," *Opt. Express*, vol. 14, no. 3, pp. 1208–1222, Feb. 2006.

[3] T. Barwicz, M. A. Popovic, P. T. Rakich, M. R. Watts, H. A. Haus, E. P. Ippen, and H. I. Smith, "Microring-resonator-based add–drop filters in SiN: Fabrication and analysis," *Opt. Express*, vol. 12, no. 7, pp. 1437–1442, Apr. 2004.

[4] B. E. Little, "A VLSI photonic platform," in *Proc. Opt. Fiber Commun. Conf.*, Washington, DC, 2003, vol. 2, pp. 444–445.

[5] J. V. Hryniewicz, P. P. Absil, B. E. Little, R. A. Wilson, and P.-T. Ho, "Higher order filter response in coupled microring resonators," *IEEE Photon. Technol. Lett.*, vol. 12, no. 3, pp. 320–322, Mar. 2000.

[6] Y. Yanagase, S. Suzuki, Y. Kokubun, and S. T. Chu, "Box-like filter response and expansion of FSR by a vertically triple coupled microring resonator filter," *J. Lightw. Technol.*, vol. 20, no. 8, pp. 1525–1529, Aug. 2002.

[7] M. A. Popovic, T. Barwicz, M. R. Watts, P. T. Rakich, L. Socci, E. P. Ippen, F. X. Kärtner, and H. I. Smith, "Multistage high-order microring-resonator filters with relaxed tolerances for high through-port extinction," presented at the Conf. Lasers and Electro-Optics, Baltimore, MD, 2005, Paper CMP2.

[8] A. Melloni and M. Martinelli, "Synthesis of direct-coupled-resonators bandpass filters for WDM systems," *J. Lightw. Technol.*, vol. 20, no. 2, pp. 296–303, Feb. 2002.
[9] M. A. Popovic, M. R. Watts, T. Barwicz, P. T. Rakich, L. Socci, E. P. Ippen, F. X. Kärtner, and H. I. Smith, "High-index-contrast, wide-FSR microring-resonator filter design and realization with frequency-shift compensation," presented at the Optical Fiber Communication Conf., Anaheim, CA, 2005, Paper OFK1.
[10] Mitsubishi Rayon America Inc. (2004). aquaSAVE Datasheet. [Online]. Available: http://www.mrany.com
[11] T. Barwicz and H. I. Smith, "Evolution of line-edge-roughness during fabrication of high index-contrast microphotonic devices," *J. Vac. Sci. Technol. B, Microelectron. Process. Phenom.*, vol. 21, no. 6, pp. 2892–2896, Nov./Dec. 2003.
[12] S. Yasin, D. G. Hasko, M. N. Khalid, D. J. Weaver, and H. Ahme, "Influence of polymer phase separation on roughness of resist features," *J. Vac. Sci. Technol. B, Microelectron. Process. Phenom.*, vol. 22, no. 2, pp. 574–578, Mar./Apr. 2004.
[13] F. Ladouceur, J. D. Love, and T. J. Senden, "Effect of side wall roughness in buried channel waveguides," *Proc. Inst. Elect. Eng.—Optoelectron.*, vol. 141, no. 4, pp. 242–248, Aug. 1994.
[14] D. Marcuse, "Radiation losses of dielectric waveguides in terms of the power spectrum of the wall distortion function," *Bell Syst. Tech. J.*, vol. 48, no. 10, pp. 3233–3244, Dec. 1969.
[15] T. Barwicz and H. A. Haus, "Three-dimensional analysis of scattering losses due to sidewall roughness in microphotonic waveguides," *J. Lightw. Technol.*, vol. 23, no. 9, pp. 2719–2732, Sep. 2005.
[16] K. K. Lee, D. R. Lim, H. C. Luan, A. Agarwal, J. Foresi, and L. C. Kimerling, "Effect of size and roughness on light transmission in a Si/SiO_2 waveguide: Experiments and model," *Appl. Phys. Lett.*, vol. 77, no. 11, pp. 1617–1619, Sep. 2000.
[17] Y. A. Vlasov and S. J. McNab, "Losses in single-mode silicon-on-insulator strip waveguides and bends," *Opt. Express*, vol. 12, no. 8, pp. 1622–1631, Apr. 2004.
[18] U. Hofmann, R. Crandall, and L. Johnson, "Fundamental performance of state-of-the-art proximity effect correction methods," *J. Vac. Sci. Technol. B, Microelectron. Process. Phenom.*, vol. 17, no. 6, pp. 2940–2944, Nov./Dec. 1999.
[19] L. Stevens, R. Jonckheere, E. Froyen, S. Decoutere, and D. Lanneer, "Determination of the proximity parameters in electron beam lithography using doughnut-structures," *Microelectron. Eng.*, vol. 5, no. 1–4, pp. 141–150, Dec. 1986.
[20] S. A. Rishton and D. P. Kern, "Point exposure distribution measurements for proximity correction in electron-beam lithography on a sub-100 nm scale," *J. Vac. Sci. Technol. B, Microelectron. Process. Phenom.*, vol. 5, no. 1, pp. 135–141, Jan./Feb. 1987.
[21] T. H. P. Chang, "Proximity effect in electron-beam lithography," *J. Vac. Sci. Technol.*, vol. 12, no. 6, pp. 1271–1275, Nov./Dec. 1975.
[22] Y. Ma, F. Cerrina, T. Barwicz, and H. I. Smith, "Theoretical and experimental study of electron beam exposure for microphotonic devices," presented at the Electron, Ion Photon Beam Technology Nanofabrication Conf., Orlando, FL, May 31–Jun. 3, 2005.
[23] S. A. Prahl. (1988). "Light transport in tissue," Ph.D. dissertation, Biomed. Eng., Univ. Texas, Austin. [Online]. Available: http://omlc.ogi.edu/pubs/pdf/prahl88.pdf
[24] C. W. Holzwarth, private communication, Apr. 2005, MIT: Cambridge, MA.
[25] T. Barwicz, "Accurate nanofabrication techniques for high-index-contrast microphotonic devices," Ph.D. dissertation, Dept. Mater. Sci. Eng., Mass. Inst. Technol., Cambridge, MA, 2005.

Tymon Barwicz was born in Warsaw, Poland, in 1977. He received the B.Eng. degree in engineering physics from the Ecole Polytechnique de Montréal, Montréal, QC, Canada, in 2000 and a joint M.Sc./Ph.D. degree in materials science and engineering from the Massachusetts Institute of Technology (MIT), Cambridge, in 2005.

He is currently a Postdoctoral Associate with NanoStructures Laboratory at MIT. His main research interest is nanofabrication of high-index-contrast microphotonic devices.

Miloš A. Popović (S'98) was born in Zaječar, Republic of Serbia, Yugoslavia, in 1977. He received the B.Sc. degree in electrical engineering from Queen's University, Kingston, ON, Canada, in 1999 and the M.Sc. degree from the Massachusetts Institute of Technology (MIT), Cambridge, in 2002. He is currently working toward the Ph.D. degree at MIT.

His research interests are theory and design of high-index-contrast photonic devices, optical resonators and filters, electromagnetic and coupled-mode theory, analytical-device models, and computational electromagnetics.

Michael R. Watts was born in Boston, MA, in 1974. He received the B.S. degree in electrical engineering from Tufts University, Medford, MA, in 1996, and the M.S. and Ph.D. degrees from the Massachusetts Institute of Technology (MIT), Cambridge, in 2001 and 2005, respectively.

He was a member of Technical Staff at The Charles Stark Draper Laboratory from 1996 to 1999. In 2001, he left Draper to continue his graduate studies.

Dr. Watts is currently a Senior Member of the Technical Staff at Sandia National Laboratories, Albuquerque, NM.

Peter T. Rakich was born in Hinsdale, IL, in 1976. He received the B.S. degree in physics from Purdue University, West Lafayette, IN, in 1999. He is currently working toward the Ph.D. degree in physics at the Massachusetts Institute of Technology (MIT), Cambridge.

His research interests include photonic crystals metamaterials and high-index-contrast integrated photonics.

Erich P. Ippen (S'66–M'69–SM'81–F'84) received the S.B. degree from the Massachusetts Institute of Technology (MIT), Cambridge, and the M.S. and Ph.D. degrees from the University of California, Berkeley, in 1962, 1965, and 1968, respectively.

He worked at Bell Laboratories, Holmdel, NJ, from 1968 to 1980 before joining the faculty of MIT, where he is currently Elihu Thomson Professor in electrical engineering and physics. His current research interests include femtosecond optical clock and arbitrary waveform technologies, ultrafast studies of materials and devices, photonic crystals, and ultrashort-pulse fiber devices.

Prof. Ippen is also a member of the National Academy of Sciences, the National Academy of Engineering, and the American Academy of Arts and Sciences.

Henry I. Smith (M'76–SM'84–F'87) received the B.S. degree in physics from the Holy Cross College, Worcester, MA, in 1958 and the M.S. and Ph.D. degrees in physics from the Boston College Graduate School Boston, MA, in 1960 and 1966, respectively.

He is a Professor in electrical engineering at the Massachusetts Institute of Technology, Cambridge, and is Director of the MIT NanoStructures Laboratory. His research interests include nanofabrication, electronic and microphotonic devices, and novel applications of nanostructures. He and his co-workers are responsible for a number of innovations, including comformable-photomask lithography, X-ray lithography, the phase-shift mask, the attenuating phase shifter, spatial phase-locked e-beam lithography, interferometric alignment, graphoepitaxy, achromatic-interferometric lithography, and a variety of quantum-effect, short-channel, single-electron, and microphotonic structures.

Prof. Smith is also a member of the National Academy of Engineering, the American Physical Society, the American Vacuum Society, the Materials Research Society, and Sigma Xi.